J Mater Sci: Mater Electron (2023) 34:1131

The green approach of ZnO NPs and its Antioxidant, hemolytic, and photocatalytic activity and functionalized r-GO-ZnO for energy storage application

Jayaprakash Meena[1,2], G. Pavithra[2], Dinakaran Anusha[2], Annamalai Senthil Kumar[1,2], and K. Santhakumar[1,*]

[1] *Nano and Bioelectrochemistry Research Laboratory, Carbon Dioxide and Green Technology Research Centre, Vellore Institute of Technology University, Vellore, Tamil Nadu 632 014, India*

[2] *Department of Chemistry, School of Advanced Sciences, Vellore Institute of Technology University, Vellore, Tamil Nadu 632 014, India*

Received: 25 October 2022
Accepted: 29 March 2023
Published online: 11 May 2023

ABSTRACT

The present paper describes the green synthesis of Zinc oxide nanoparticles (ZnO NPs) from the flowers of *L. nepetifolia*. Zinc oxide nanoparticles have gained more interest from researchers due to their wide applications from biological activity to energy storage system. The synthesis of ZnO nanoparticles and examined by using Ultraviolet–visible spectroscopy, Fourier Transform-Infrared spectroscopy, X-ray Diffraction analysis, Dynamic Light Scattering analysis, Raman spectroscopy, Scanning Electron Microscopy and Energy Dispersive X-ray spectroscopy, BET, XPS, Transmission Electron Microscopy, and Thermogravimetric Analysis. The photocatalytic studies were followed using methylene blue (MB) dye by ZnO nanoparticles by using sunlight as a source. The degradation of MB dye is found to be 90% within 70 min. Then the synthesized ZnO nanoparticles help to evaluate the antioxidant activities against Nitric oxide, Hydrogen peroxide, and DPPH free radicals. Moreover, the synthesized ZnO NPs show good biocompatibility nature, and the electrochemical analysis of reduced Graphene Oxide with Zinc oxide (rGO-ZnO) nanocomposite shows that the prepared rGO-ZnO nanocomposite has a high specific capacitance of about 667 F g^{-1} in comparison with the pure Zinc oxide nanoparticles (200 F g^{-1}) and has good cycling stability over 1000 cycles.

Address correspondence to E-mail: ksanthakumar@vit.ac.in

https://doi.org/10.1007/s10854-023-10373-2

1 Introduction

Environmentally friendly nanoscience research is one of the integrative research domains, in various sectors. The synthesis of nanoparticles can be done by several methods such as the sol–gel process, pulsed laser deposition, thermal evaporation, mechanical milling method, spray pyrolysis, and organometallic microwave-assisted methods [1]. Unfortunately, those methods are highly expensive, the usage of toxic chemicals is high, labor-intensive (need a large workforce), and dangerous to the environment. Some hazardous chemicals involved in the chemical methods have harmful effects in the medical field. However, the green synthesis of metal nanoparticles using bio waste which encourages the non-toxic, eco-friendly pathway to the synthesis of nanomaterial [2–4]. Especially agricultural wastes contain a high number of secondary metabolites which reduces metal ions by biologically active substances like an enzyme, amino acid, phenolic compound, and vitamin which all acts as natural reducing agents. Using agro-waste materials lowers the cost of synthesis and minimizes the energy needed when compared to both methods (physical or chemical) also, they lower the need for using highly dangerous chemicals or other byproducts, these properties highlighting the essence of the green route synthesis method by using natural wastes of biological or plants like seed, barks, leaf, flower, stem, etc. [5–7]. There are various metal NPs like ZnO, TiO_2, WO_3, CuO, Fe_2O_3, SnO_2, and CeO_2 that plays a versatile role in all domain such as photocatalyst, and energy storage application. Metal oxides nanoparticles (MONPs) are crucial in various diverse applications, such as energy generation, conversion, and storage, as well as in environmental remediation and pollutants monitoring. In MONPs exhibit a variety of their crystal structure, morphology, composition, intrinsic flaws, doping, etc., metal oxides demonstrate a wide range of functional qualities that affect their optical, electrical, chemical, and catalytic activity [8]. Among various metal oxide nanoparticles, ZnO nanoparticles have wide applications in various sectors due to their strong UV protection, optoelectronic devices, energy storage devices, removal of heavy metals from water, and in the medical fields such as nano diagnostics, nanomedical, gene, and drug delivery, and high antimicrobial activities [6–14]. In recent years, the simplistic and new synthetic procedure of ZnO nanoparticles is increased due to its non-poisonous, multiple functions, is highly biocompatibility, very low cost, and eco-friendly nature over other metallic nanoparticles [15, 16]. Over the decades, various methods of synthetic procedure are followed to synthesize ZnO NPs, especially the synthesis of ZnO using a greener method was trending due to its simple and easy procedure.

Leonotis nepetifolia is a tropical African and Southern Indian flower belonging to the family Lamiaceae. Therefore *L. nepetifolia* flowers are cost-less agro-waste that contains secondary metabolites, during the biogenesis of metallic nanoparticles they could additionally act as reducing agents, capping agents, and stabilizing agents in a very simple and cost-effective synthesis method [9]. The active ingredients of *Leonotis nepetifolia* like polyphenols, tannins, and flavonoids will carry out reduction/oxidation reactions to convert metal precursors into specific metal nanoparticles. Bioreduction processes are chemically complex but environmentally safe and good. The main highlight of this work investigates the biosynthesis of ZnO NPs from *Leonotis nepetifolia* extract and the synthesized ZnO NPs were characterized by XRD, UV–Vis, FT-IR, DLS, SEM, EDX, TEM, TGA, BET, XPS and Raman spectroscopy and the basic structural properties were disclose in Table 1 and the

Table 1 structural properties of ZnO

Property	Measured value
Crystal structure	Hexagonal, Wurtzite
Crystal	Noncentrosymmetric
Molecular weight	ZnO:81.38 g/mol
Weight %	O:19.66, Zn: 80.34
Atomic %	O:50.00, Zn:50.00
Lattice constant	a = 3.246 Å
	c = 5.207 Å
α	90°
β	90°
γ	120°
Space group	P63mc (186)
Density	5.67 g/cm^3
Melting point	Tm = 2250 K
Band gap at RT	3.3 eV
Size:	XRD-26 nm
	SEM-25-35 nm
	TEM-25-100 nm
Stress (ε)	0.00243
Strain (σ)/10^9 Pa	0.568

synthesized ZnO NPs were applied for various applications like antioxidants, dye degradation, biocompatibility, and energy storage applications. ZnO NPs exhibited 3.5% of total hemolytic activity and there was no destruction of red blood cells. The hemolytic activity of synthesized ZnO nanoparticles was less considerable, implying its safe nature in the chemotherapeutic application. The photocatalytic studies were followed using methylene blue (MB) dye by ZnO nanoparticles by using sunlight as a source. The degradation of MB dye is found to be 90%. The synthesized ZnO NPs show good biocompatibility nature and natural antioxidant activity against DPPH, nitric acid, and H_2O_2 radicals. Importantly, the synthesized ZnO with r-GO shows acceptable supercapacitor applications with high specific capacitance (667 F g^{-1}) and high cyclic stability. This implies the biosynthesized ZnO shows various applications in greener methods. The highlight of this work is one pot synthesized greener method material for various applications like photocatalyst, dye degradation, and energy storage application.

2 Experimental part

2.1 Materials

The chemicals $Zn(NO_3)_2$, distilled water, and other reagents used in this work were purchased from Sigma-Aldrich and used without any purification.

2.2 Process and preparation of the extract

The flower extract was prepared by the following process, the *L. nepetifolia* flower was washed many times with water and dried under sunlight. Approximately 10 g of *L. nepetifolia* dried flowers were taken in a washed 250 mL beaker and mixed with 100 mL of H_2O (double-distilled water). Then the mixtures were boiled at 100 °C for around 10 min. Afterward, the solution color changes from colorless to reddish-brown. Afterward, the flower extract is transferred to Whatman No. 1 filter paper and then that filtrate was kept in the refrigerator for further usage. Finally, it is used for the synthesis of Zinc oxide nanoparticles.

2.3 Biosynthesis of ZnO nanoparticles

The Zinc oxide nanoparticles were synthesized by mixing *L. nepetifolia* flower extract (50 mL) and zinc nitrate (5 g) and then that mixture was stirred using the magnetic stirrer at 60–80 °C for 1 h. We obtain a reddish paste when the temperature reaches 70 °C, this paste is dried in the dryer at 100–130 °C, for 45 min in the oven. Zinc oxide nanoparticles were obtained in the form of pale yellow-colored powder. Then, it is collected and dehydrated at 70 °C utilizing a hot air oven overnight. Finally, it is stored in a vacuum desiccator.

2.4 Purification of ZnO nanoparticles

To recover the ZnO nanoparticles, the *L. nepetifolia* flower extract (10 mL) was mixed with the zinc nitrate solution (90 mL). Afterward, that mixture was placed at room temperature for nearly 4 days and then the nanoparticles formed were visually observed at regular intervals of time. After completing the incubation, the solution was allowed to centrifuge at 5000 rpm for 15 min. Then the precipitate was collected and suspended in distilled water for further centrifugation. The collected precipitate was washed two to three times to remove the impurities present in it. Finally, the nanoparticles obtained were dried in an air oven overnight till the moisture is fully discarded and the dried nanoparticles were collected for further use.

2.5 Characterization

The Ultraviolet–Visible absorption (UV–Vis) spectrum of the sample was collected by using the Jasco (V-560) spectrometer with a wavelength of 200—800 nm. The Fourier transform infrared (FT-IR) spectrum of the synthesized ZnO nanoparticles was obtained from the 460 Plus FT- IR spectrometer (JASCO) instrument. The identification of the phase of the annealed powdered nanoparticle is recorded by using the JEOL JDX 8030 X-ray diffractometer instrument of Cu—K $\propto$ with radiation of 1.5406 A°. The particle size was measured by a dynamic light scattering (DLS) analyzer [ZEN3600 He–Ne laser (633 nm), the size ranges from 0.3 nm to 10 mμ]. Raman spectrum was carried out by using LabRAM HR evolution microscopic confocal Raman spectrometer (Horiba, Japan). The scanning electron

microscopy (SEM) studies and Energy Dispersive X-ray (EDX) spectroscopy were recorded by using FE-SEM, SU8000, Hitachi, Tokyo, Japan. Transmission Electron Microscopy (TEM) analysis was performed on the FEI TECNAI T20 G2 instrument operated at an acceleration voltage of 120 kV. Thermal analysis and decomposition of the synthesized nanoparticles are observed by the differential scanning calorimetry/thermogravimetric analysis (DSC/TGA-50, SHIMADZU) measured from 25 to 700 °C at a heating rate of 10 °C/min. The Brunauer–Emmett–Teller (BET) specific surface area of ZnO NPs was measured by adsorption–desorption study of nitrogen molecules at 77 K using a Quanta chrome Nova 1000 analyzer. The surface composition and chemical state of the ZnO NPs were determined by XPS (ThermoScientific, MULTI LAB 2000).

2.6 Photocatalytic degradation of MB by ZnO NPs

The synthesized ZnO was thoroughly investigated for bioremediation studies performed by using methylene blue ($C_{16}H_{18}ClN_3S$) in direct sunlight. During the reaction, the flux in lighting was studied at the starting point of the analysis it was 1225 W/m^2 and then it reaches 1275 $W/m.^2$ for 70 min. The light intensity was determined to be the same all over the study. 0.3 g of synthesized ZnO nanoparticles and dissolved in 50 mL of 10 µM dye solution (MB dye) and then sonicated for 25 min in the darkroom to attain maximum absorption. Likewise, the control was kept under the same condition without ZnO, then it changes the colour of the dye solution when compared with the nanoparticles [16, 17]. The colour of the solution (MB) was changed from blue to colourless. For methylene blue, the UV absorption peak was obtained at 660 nm for 10 min intervals [18]. According to the following formula, the degradation percentage of the dye can be calculated by using the Eq. (1)

$$\%\,\text{degradation} = (I_0 - I/I_0) \times 100 \quad (1)$$

where, I_0 is the starting intensity of the MB,
I is the intensity after photodegradation.

2.7 Haemolytic activity

Haemolysis is defined as the destruction of red blood cells (RBC) which causes the release of hemoglobin into the blood plasma due to the damage to the erythrocyte membrane. Then, hemolysis takes place in a higher area which leads to a very dangerous pathological condition. 9 mL of the Heparinized human blood sample was collected; 1.5 mL of 3.9% sodium citrate was dissolved slowly. Afterward, this can highly inhibit blood coagulation. Then the rejection of supernatant having platelet-poor plasma occurred. Once the plasma is discarded, it was washed thrice with 10 mL of PBS (phosphate buffer saline) solution having a pH value of 7.4 to separate the RBC buffy coat. The suspension of cells in PBS takes place to get the cells suspended uniformly. Different concentrations of ZnO nanoparticles of untreated RBCs, 25, 50, 75, 100, and 125 gμ/mL were taken in separate sample tubes. Add 2 mL of erythrocyte suspension to all the test tubes and the sample tubes were reversed. Then sample tubes were shaken slowly to keep the blood in contact with synthesized ZnO nanoparticles and simultaneously incubated at 36 ^{0}C for 85 min [19]. Centrifugation of the sample occurred at a high 3000 rpm of around 6 min. Separation of the supernatant was taken place and 540 nm is the absorbance measured against a PBS blank solution. Triton X-100 (0.1% v/v) and PBS were used as positive and negative control respectively. Haemolysis percentage (%) was calculated by the formula (2) shown below

$$\text{Haemolysis percentage} = \frac{(\text{The absorbance of sample} - \text{Absorbance of blank})}{(\text{Absorbance of positive control})} \times 100 \quad (2)$$

2.8 Antioxidant activity of synthesized ZnO NPs by flower extract

2.8.1 *Nitric oxide scavenging assay*

Nitric oxide scavenging assay of *L. nepetifolia* was determined by Griess reaction using sodium nitroprusside and Griess reagent used as an important ingredient. 100 μ L of 10 mM sodium nitroprusside dissolved in 100% of CH_3OH (Methanol) was added slowly to various concentrations of flower extract *(L. nepetifolia)* and synthesized NPs (ZnO NPs) [(20–100 gμ/mL)]. Ascorbic acid has been utilized as a standard. The prepared reaction mixture was placed at RT (Room Temperature) [(20–25 °C)] for nearly 3 h. After incubation, the reactant absorbance was

determined at 546 nm and the scavenging rate is calculated by using the formula (3).

2.8.2 H_2O_2 scavenging assay

The H_2O_2 scavenging assay of *L. nepetifolia* was estimated by monitoring the reduction of H_2O_2. Ascorbic acid was considered as a standard and various concentrations of *L. nepetifolia* flower extract or ZnO NPs (20–100 gμ/mL) is dissolved in dH_2O (Distilled water) and were mixed in an H_2O_2 solution,600μ L of 40 mM in PBS. After the incubation process, the reactant absorbance was determined at 230 nm and the scavenging rate is calculated by using the formula (3).

2.8.3 DPPH scavenging assay

DPPH compound is a free radical which is used as a substrate to measure antioxidant activity. The reduction capacity of DPPH free radical was measured by the decrease in its concentration induced by the antioxidant activity. The free radical scavenging potential of the flower extract, antioxidant was observed by the degree of discoloration [20, 21]. The antioxidant activity of flower extract (*Leonotis nepetifolia*) and synthesized ZnO NPs was estimated by DPPH free radical scavenging activity. 1 M DPPH solution of 500 μ L is mixed in 100% of methanol and then it was added equally to different concentrations of L. nepetifolia flower extract and ZnO NPs (20–100 gμ/mL). Afterward, shake the solution vigorously and then place that solution for nearly 30 min of incubation in a dark place. After the completion of incubation, the reactant absorbance was determined at 517 nm [22, 23]. Ascorbic acid was utilized as a positive control.

The percentage of scavenging potential was measured by the formula given below

$$\text{Scavenging activity}\,(\%) = \left[\left(A_{\text{control}} - A_{\text{sample}}\right) / A_{\text{control}}\right] \times 100 \tag{3}$$

where A $_{\text{control}}$ = Absorbance of a control, A $_{\text{sample}}$ = Absorbance of a sample.

2.9 Preparation of rGO/ZnO nanocomposite

About 0.3 g of ZnO NPs and rGO of 1 g were mixed with 100 mL of distilled water (dH_2O) and it is placed at ultrasonication for 30 min with constant stirring. Then the mixture obtained is filtered and dried in a dried oven. The nanocomposite (rGO/ZnO) obtained was stored in the vacuum desiccator under a nitrogen atmosphere.

2.10 Electrochemical measurements

CHI electrochemical workstation (Model 660E, USA) with typical three types of electrodes was used to perform the electrochemical analysis in a 2 M KOH electrolyte solution. For electrochemical characterization, CV (Cyclic voltammetry), EIS (Electrochemical impedance spectroscopy) and CP (Chronopotentiometry) were used [24–26]. A platinum wire is used as a counter, a saturated calomel electrode as a reference and an active material coated with nickel foil as the working electrode. About 90 wt% of this active material, 5 wt% of acetylene black and 5 wt% of polytetrafluoroethylenes were ground and mixed with N-methyl-2-pyrrolidone (NMP) to get a homogeneous slurry. Then using a doctor blade method, the slurry is coated uniformly on a nickel foil (1 cm^{-2}) and dried for 12 h at 90 °C. The mass of the active material contains 5 mg and acts as a working electrode. Around 0.01 Hz–100 k Hz of frequency range and with 10 mV of the sinusoidal signal, the EIS was conducted. Then, with 5 A g^{-1} of current density, we tested the cycling stability [27–29]. From the data of CV and GCD, the Energy density (d_e, Wh kg^{-1}), average Power density (d_p, W kg^{-1}) and Specific capacitance (F g^{-1}) were calculated using the following formulas (4–7):

$$SC(CV) = \frac{\int Idv}{vm\ \Delta V} \tag{4}$$

$$SC(GCD) = \frac{I\ X\ \Delta t}{m\ X\ \Delta V} \tag{5}$$

$$d_e = \frac{SC_s \times (\Delta V)^2}{2} \tag{6}$$

$$d_p = \frac{d_e}{\Delta t} \tag{7}$$

where m is the mass of active materials (g),

I is the current load (A g^{-1}),v is the scanning rate, ΔV is the potential difference, and.
Δt is the discharge time.

3 Results and discussion

3.1 UV–Visible spectroscopy

UV–Vis (Ultraviolet–Visible) spectroscopy is the technique commonly used to determine the optical properties of the nanoparticle, and it also explains the formation of ZnO nanoparticles in an aqueous solution. Figure 1a shows the UV–Vis spectra of extract and synthesized ZnO NPs. The absorption spectrum of *Leonotis nepetifolia* flower extract showed a peak at the wavelength of 275 nm which corresponds to components like glycosides that can be used as a capping agent and flavonoids as a reducing agent for the synthesis of Zinc Oxide nanoparticles. The absorption spectrum of the ZnO NPs showed single broadband at the wavelength of 340 nm. This peak is assigned as the transition of electrons from the valence band (VB) to the conduction band (CB) ($Zn_{3d} \rightarrow O_{2p}$). Due to its blue shift, the reduction in the size of the ZnO nanoparticle causes a decrease in the wavelength and increases the frequency. Thus, ZnO nanoparticles absorb at a lesser wavelength than that bulk ZnO. The free electrons in ZnO nanoparticles give rise to the Surface plasmon Resonance (SPR) absorption band, which occurred due to the combined vibration of electrons present in the nanoparticles with the light waves. These SPR thin peaks show that the particles are in a nanosized range with narrow particle size distribution.

The SPR (Surface Plasmon Resonance) and energy bandgap (E_g) of the green synthesized ZnO nanoparticles were calculated with the wavelength range of 200–800 nm using the UV–Visible spectroscopic method. ZnO nanoparticles were dispersed in distilled water (200 mg $L.^{-1}$) and exposed to an ultrasonic bath for 15 min [30, 31]. The bandgap energy of ZnO nanoparticles is calculated by using the formula (8)

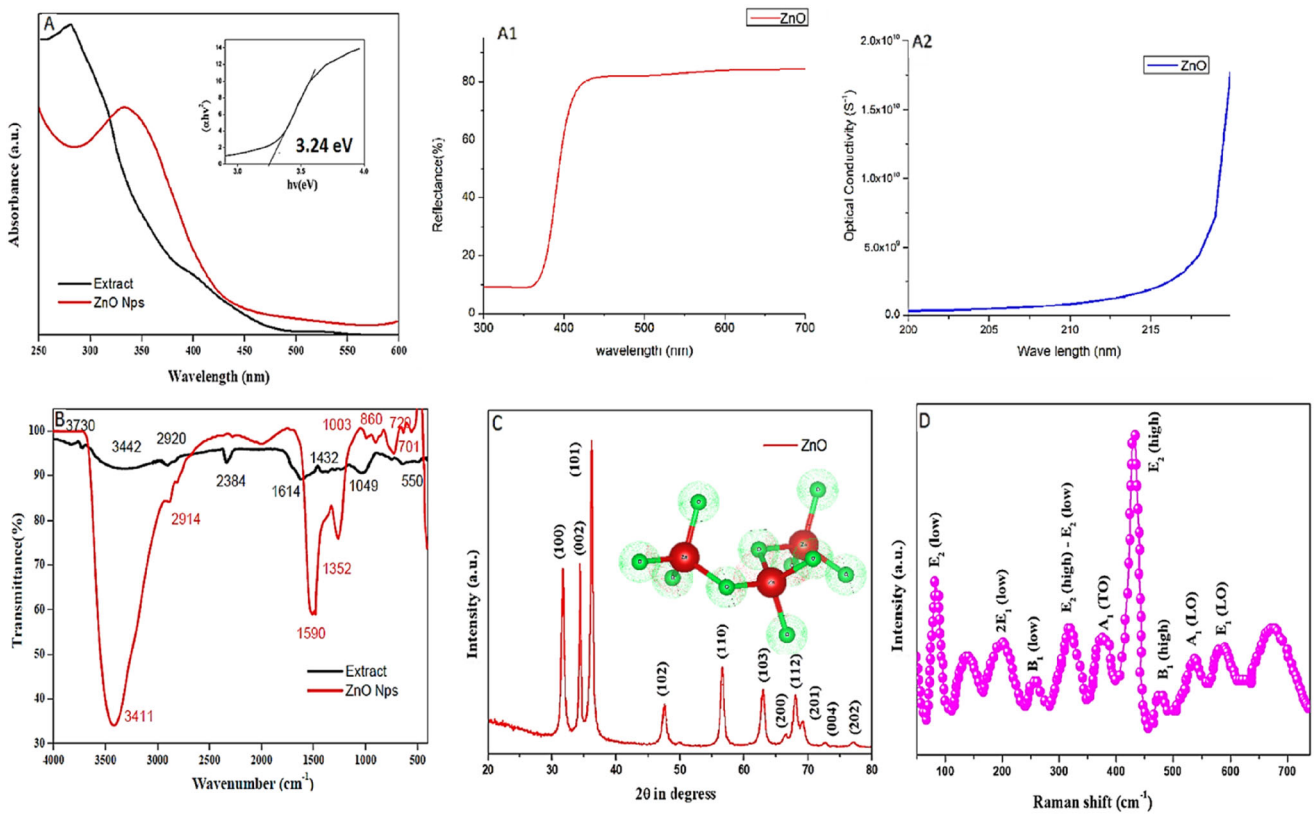

Fig. 1 **a** UV–Vis absorption (Inset Tauc's plot of ZnO) (a1) Reflctance (a2) optical conductivity **b** FT-IR spectrum **c** XRD pattern of synthesized ZnO NPs **d** Raman spectrum of synthesized ZnO NPs

$$E = hc/\lambda \quad (8)$$

where h—Planck constant (6.626×10^{-34} J s),c—velocity of light (2.99×10^{8} m s^{-1}), andλ_{max}—maximum absorption wavelength.

The bandgap energy calculated using the above formula for ZnO NPs was determined to be 3.24 eV (Fig. 1a) is smaller when compared to bulk ZnO (3.3 eV). The diffused reflectance spectra (Fig. 1A1) implies a sudden increase at 380 nm it shows the material had a good reflective characteristic and the intrinsic property of material can define by optical conductivity which shows the conduction nature from the movement of charge because of alternating electric field of incident light and the optical conductivity was calculated by using below Eq. (9 and 10) (Fig. 1A2)

$$n = \frac{1}{Ts} + \sqrt{\frac{1}{Ts} - 1} \quad (9)$$

$$\sigma_{opt} = n\alpha c/4\pi \quad (10)$$

Which represents σ_{opt} is optical conductivity, n is refractive index, α is adsorption coefficient, Ts is transmittance, and n is reflectance.

3.2 FT-IR spectroscopy

FT-IR studies are an analytical technique widely used to detect various functional groups, ionic interaction, and metal–oxygen bonds that exist in Leonotis nepetifolia flower extract and the synthesized ZnO nanoparticles. Figure 1b shows the spectra for extracted and synthesized ZnO NPs. Strong stretching at 3730 cm^{-1} corresponds to the sharp OH stretching frequency of alcohol. The broad stretching peak at 3442 cm^{-1} and 3411 cm^{-1} is due to the OH group for the extract and ZnO NPs. The peak at 2920 cm^{-1} and 2914 cm^{-1} is due to the—CH stretching frequency of the hydroxyl compound. The strong absorption peak at 2384 cm^{-1} corresponds to the stretching vibration of O=C=O. The peak at 1614 cm^{-1} and 1590 cm^{-1} is mainly due to the stretching vibration of C=C of the alkene group. Few absorption peaks at 1352 cm^{-1}, 865 cm^{-1}, and 1432 cm^{-1} have been attributed to—CH stretching frequency. The absorption peak at 1003 cm^{-1} corresponds to the C–N bond stretching frequency of the primary amine of the ZnO NPs. The peak at 720 cm^{-1} and 701 cm^{-1} might be due to C–H out-of-plane bending. A stretching peak of 1048 cm^{-1} appears due to the stretching frequency of C–O vibration. The peaks at 550 cm^{-1} and 500 cm^{-1} correspond to the stretching vibration of Metal–Oxygen (Zn–O) [32–34].

3.3 XRD analysis

X-Ray Diffraction studies are used to measure the crystalline nature of synthesized ZnO powder. The XRD pattern of the synthesized nanoparticles was shown in Fig. 1c. XRD studies were used to determine the crystal phase of the nanoparticles (JCPDS 36–1451). The intense peaks were observed 2 $\theta from 20-80$. XRD pattern shows an intense peak obtained 2 θ values at 31.68°, 34.51°, 36.27°, 47.68°, 56.55°, 63.05°, 66.68°, 68.11°, 69.21°, 73.02°, 77.16° are due to corresponding diffractions from the lattice planes (h, l, k) are (100), (002), (101), (102), (110), (103), (200), (112), (201), (004), (202) respectively confirms the hexagonal wurtzite structure [35–37]. The particle size of synthesized ZnO NPs can be measured by Debye–Scherrer,s formula (11),

$$D = \frac{K\lambda}{\beta \cos\theta} \quad (11)$$

where D—Particle size of the nanoparticlesK—Scherrer, s constant.λ—Wavelength of the X-rayβ—Additional peak width at half the peak height.θ—Bragg angle

This equation is used to determine the *crystallite size of about 26 nm. The sharp and narrow diffraction peak observed at (101) was 26 nm*. The crystallinity of the synthesized ZnO nanoparticle was confirmed by the narrow peak. The XRD pattern does not show any other impurity peak indicating the high purity of wurtzite ZnO nanoparticles are prepared. the lattice parameters a and c for the synthesized wurtzite ZnO structure were calculated using the equation.

3.4 Dynamic light scattering analysis

DLS analysis is a non-invasive technique widely used to measure the particle-size distribution (PSD) of macromolecules and small particles in dilute suspension using a narrow laser beam and scattering of light is noticed by a fast single-photon detector at a well-known scattering angle θ. The initial measurement of DLS has performed with the intensity-weighted particle with clearly defined PSD. The particle size starts from 20 to 25 nm and the average

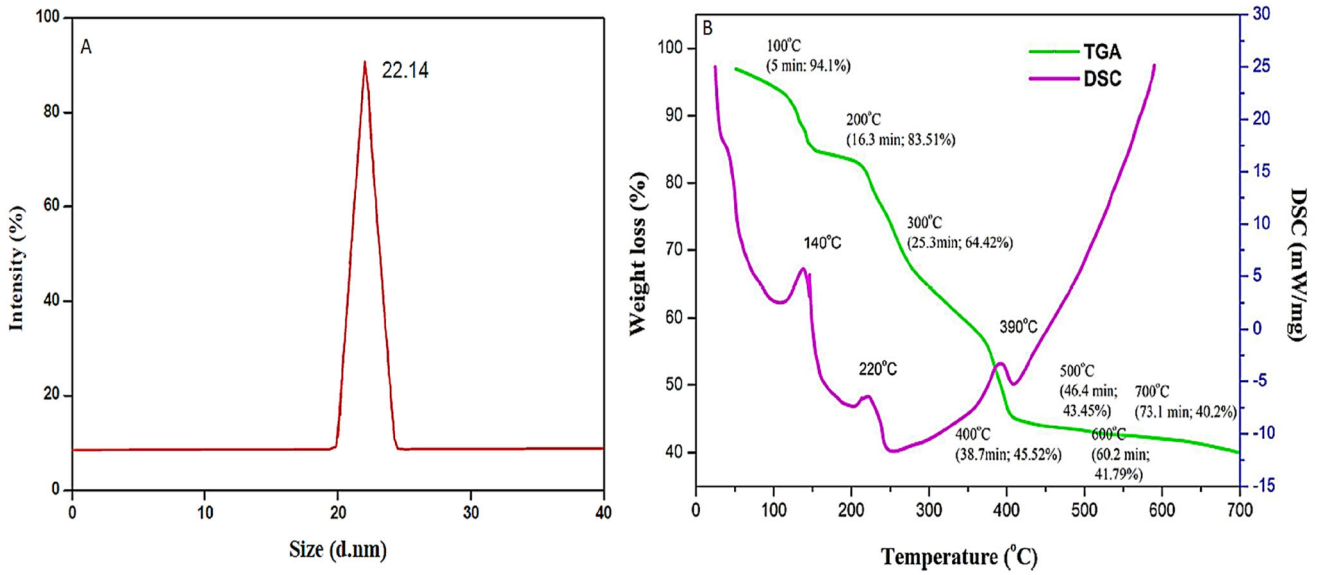

Fig. 2 **a** Particle size analysis of ZnO nanoparticles **b** TGA/DSC of green synthesized ZnO NPs (Color figure online)

particle size of ZnO nanoparticles in an aqueous medium is 22.14 nm (Fig. 2a). The DLS results showed a single peak and narrow distribution at room temperature. In DLS analysis comparative radial symmetry of size distribution images show the uniformity of the synthesized ZnO NPs [38, 39]. The particle size measured using the DLS method was also supported by XRD analysis (25.68 nm).

3.5 Raman analysis

Raman spectra of the synthesized nanoparticles were shown in Fig. 1d. The Raman spectrum is important to determine the crystallization process, vibrational property, structural disorder, and defects in nanostructures. The Raman spectra are used to obtain the vibrational properties of synthesized ZnO nanoparticles. As stated in the group theory, the given formula (12) is used to measure the optical modes.

$$\Gamma\text{opt} = \text{A1} + 2\text{B2} + \text{E1} + 2\text{E2} \quad (12)$$

where A1 and E1 are the modes of two active polar branches, it is split into Longitudinal Optical (LO) and Transversal Optical (TO) components with various frequencies. A1, E1, and E2 are the modes of the first-order phonon. Both the phonon modes (A1 and E1) obtained are polar and both seem to be Raman and infrared (IR) active whereas the mode (E2) is non-polar and Raman active only [40, 41]. The first-order Raman modes were obtained at 90 cm^{-1}, 380 cm^{-1}, 420 cm^{-1}, 540 cm^{-1}, 582 cm^{-1}, and 680 cm^{-1} which represents to the E_2(low), A_1(high), E_2(high), A_1(LO) and E_1(LO) respectively. The second-order phonon has presented at about 200 cm^{-1} that is assigned to $2E_1$(low). Finally, the multiphoton mode was obtained at 330 cm^{-1} which corresponds to E_2(High)—E_2(low).

3.6 SEM and EDX analysis

The SEM image of the synthesized nanoparticles was shown in Fig. 3c. The shape and size of synthesized ZnO nanoparticles can be determined by this analysis. The different magnifications range from 2 to 200 µm are seen through SEM images. Most of the ZnO nanoparticles are spherical with high agglomeration observed and the average particle size from 25 to 35 nm is confirmed by SEM images and matches with the XRD crystallite size. The single nanoparticles cannot be considered by the intense observation of the SEM images. Then synthesized ZnO nanoparticles are analysed by EDX (Energy-Dispersive X-ray) spectroscopy (Fig. 3d). The elemental composition of the ZnO nanoparticles is determined by the EDX analysis. EDX analysis verified the existence of synthesized ZnO NPs. Using EDX the presence of components such as zinc (76.26%), oxygen (20.51%), and carbon (3.23%) is determined. EDX results indicate that there is a variation from stoichiometry, when we consider the atomic weight of the elements, then we obtain the number of oxygen than zinc. But the synthesized ZnO was not stoichiometric, it can be known by these

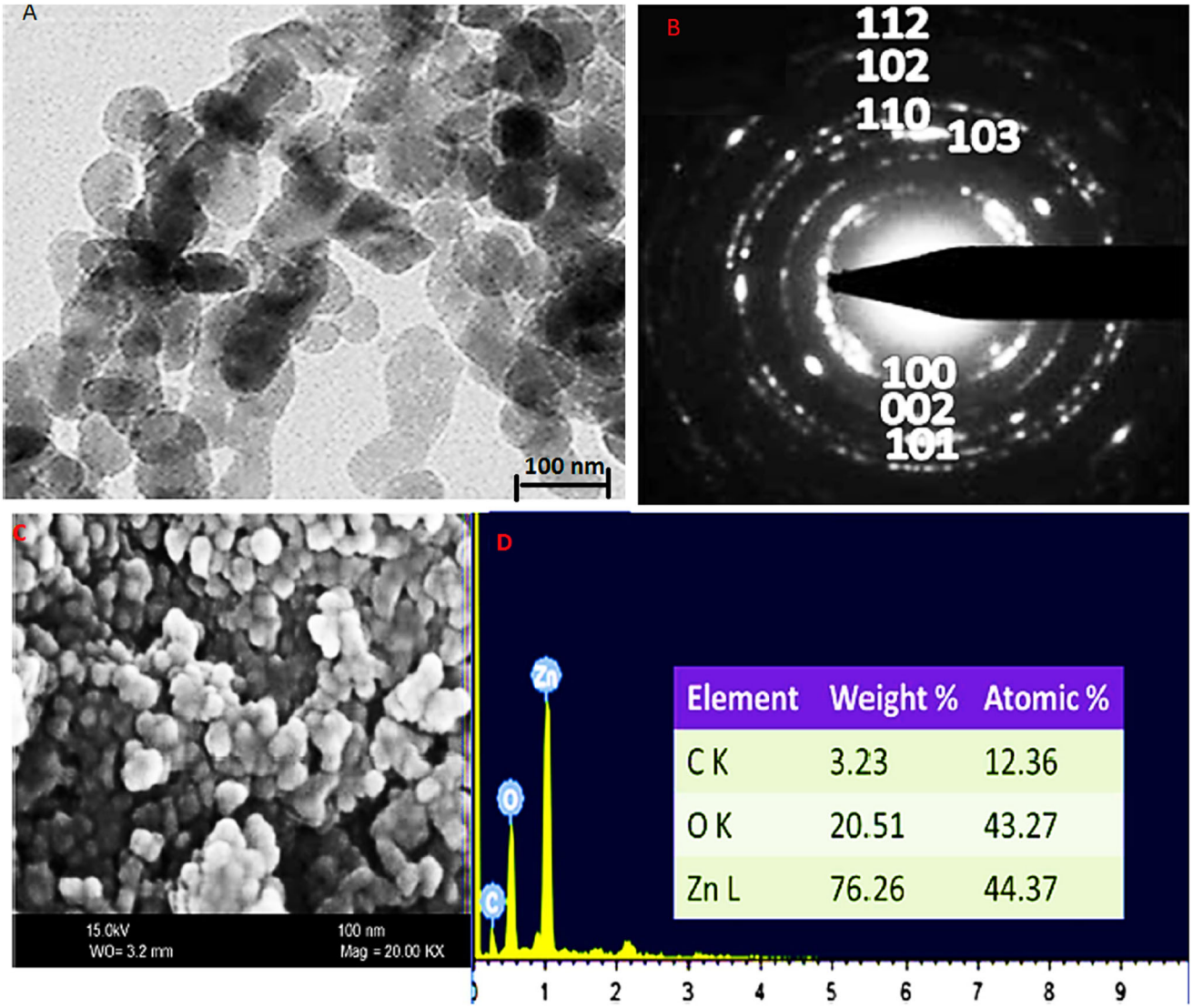

Fig. 3 **a** TEM image of synthesized ZnO NPs **b** SAED pattern with (*h, k,l*) values **c** SEM of ZnO **d** EDAX analysis showsing the elemental composition of synthesized of ZnO

percentages and then presented defects, mostly interstitial oxygen (O_1) gives the excess of this element in the sample. A strong signal is revealed for zinc by EDX spectra. Carbon is present in very low amounts which indicates the action of plant phytochemical groups in the reduction process and capping method of the synthesized ZnO nanoparticles. No other elements were determined, this shows the pure ZnO nanoparticles obtained by green synthesis [42, 43].

3.7 TEM analysis

Figure 3a indicates the TEM image of the synthesized nanoparticles. Variations of the particle shape or the presence of larger or smaller particles are directly visualized by the TEM images. The size and morphology of the synthesized ZnO nanoparticles were studied using TEM. TEM images show irregularly shaped nanoparticles with a distribution of agglomerates. TEM images revealed that the ZnO nanoparticle was mostly spherical with size ranges from 25 to 100 nm coinciding with the XRD crystallite size. Due to green synthesis, some shapes were oval, where the biological molecules can act as capping on ZnO nanoparticles. Then X–rays intensities which are dispersed by a sample as a function of the scattering angle are measured by a technique known as SAED For the homogeneous sample, reliable results based

on the evaluation of the excess number of particles are obtained by an ideal method SAED (Fig. 3b). More accurately, reveals a polycrystalline structure mainly as per the observed diffraction rings (100), (002), (101), (102), (103), (110), (112). It is observed that the most intense diffraction ring at (100) and coincides with the XRD data [44, 45].

3.8 Thermogravimetric and differential scanning calorimetry analysis

The TGA of the synthesized nanoparticles was shown in Fig. 2b. The thermal analysis technique is used to determine the physical changes of the substance at a controlled temperature. Thermogravimetric analysis (TGA) is a technique used to characterize the material by measuring its change in mass as a function of temperature. The transfer of heat in the sample is determined by DSC (Differential Scanning Calorimetry) analysis (Fig. 2b). TGA / DSC analysis of synthesized nanoparticles provides concurrent weight change, and heat flow respectively on the same sample. From the TGA diagram of ZnO NP, three stages of weight loss can be detected. The first weight loss of about 5–10% that had been reported from 25 to 120 °C is because of the evaporation of water molecules in the sample. The simultaneous second weight loss of around 20–30% was observed in the range of 120–210 °C and is attributed to decarboxylation. The third weight loss of about 210–350 °C indicates the formation of ZnO NP. No weight loss recorded between 350 and 700 °C was seen in the TGA curve, which indicates the ZnO nanoparticles formed as a final product. Three quasi-sharp endothermic peaks were recorded from the DSC analysis. The first endothermic peak observed at 140 °C was attributed to the evaporation of the water absorbed from the sample and the second endothermic peak at 220 °C is due to the decomposition of organic molecules present in the sample. The third endothermic peak at 390 °C is due to the decomposition of the precursor to ZnO NP [46, 47].

3.9 Elemental composition of synthesized ZnO NPs

The further conventional method to investigate the surface chemical properties of synthesized ZnO NPs was subjected to X-ray photoelectron spectroscopy as shown in Fig. 4. The wide scan survey shows the

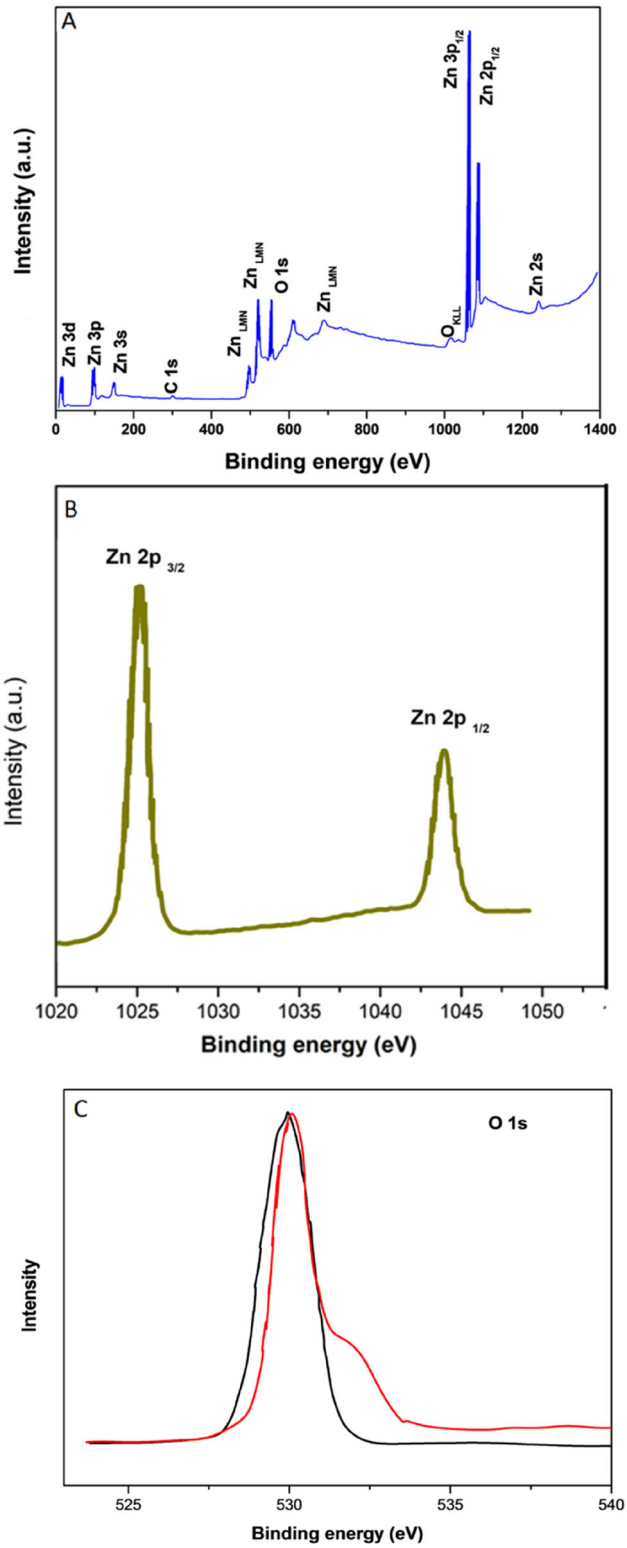

Fig. 4 XPS spectra of ZnO with a scan range of 0 to 1400 eV binding energies **a** wide scan; **b** Zn 2p region of ZnO NPs **c** O 1 s region in ZnO NPs

presence of Zn and O in the synthesized ZnO NPs. In Fig. 4b the peaks observed at 1024 and 1044 eV represents Zn $2P_{3/2}$ and Zn $2P_{1/2}$ this discloses the presence of Zn in the state of Zn^{2+}. Similarly, in Fig. 4c the binding energy at 529 eV and 531 eV represents O 1 s of O^{2-} ion in the Zn–O bonding those values were matched with Asha Rani et al. [48].

3.10 Textural surface analysis

According to Brunauer Emmett Teller (BET), the surface area of synthesized ZnO nanoparticles was examined to identify the surface chemical properties and porosity of the material. Figure 5 represents the N_2 adsorption and desorption isotherm of ZnO nanoparticles and it represents the type IV isotherms behavior with the H-3 hysteresis loop as per IUPAC classification, exhibiting mesoporous materials, with pore openings from 2 and 50 nm [48] and the pore size distribution was inset into the Fig. 5. Using Brunauer–Emmett–Teller (BET) surface area analysis, the surface area of ZnO nanoparticles was determined to be $62.1 m^2/g$.

3.11 Photocatalytic activity of MB

The absorption spectrum of the MB polluted sample at various intervals of photocatalytic activity is shown in Fig. 6a. The photocatalytic activity was carried out for methylene blue (MB) using the flowers of Leonotis nepetifolia, and ZnO nanoparticles were synthesized. The natural light source was taken from the sun and the absorption spectra at 660 nm are obtained for methylene blue. The initial step involves MB dye molecules being adsorbed on ZnO nanoparticles which results in the dye sensitization of ZnO. Through UV light, the VB (Valence Band) contains electrons (e^-) of highly dye-sensitized ZnO and gets excited to the CB (Conduction Band) with equal amounts of h^+ (holes) produced in the Valence Band. The more positive potential is found in the Conduction Band of ZnO, the superoxide are produced by the reactions of oxygen molecules, and the surface electrons. The separated h^+ (holes) will interact with the H_2O (electron donors) forms active·OH, few free radicals. Following, the attack of surface-adsorbed MB dye molecules with the produced h^+ and other free radicals (·OH, $O_2{}^{\cdot -}$), gives

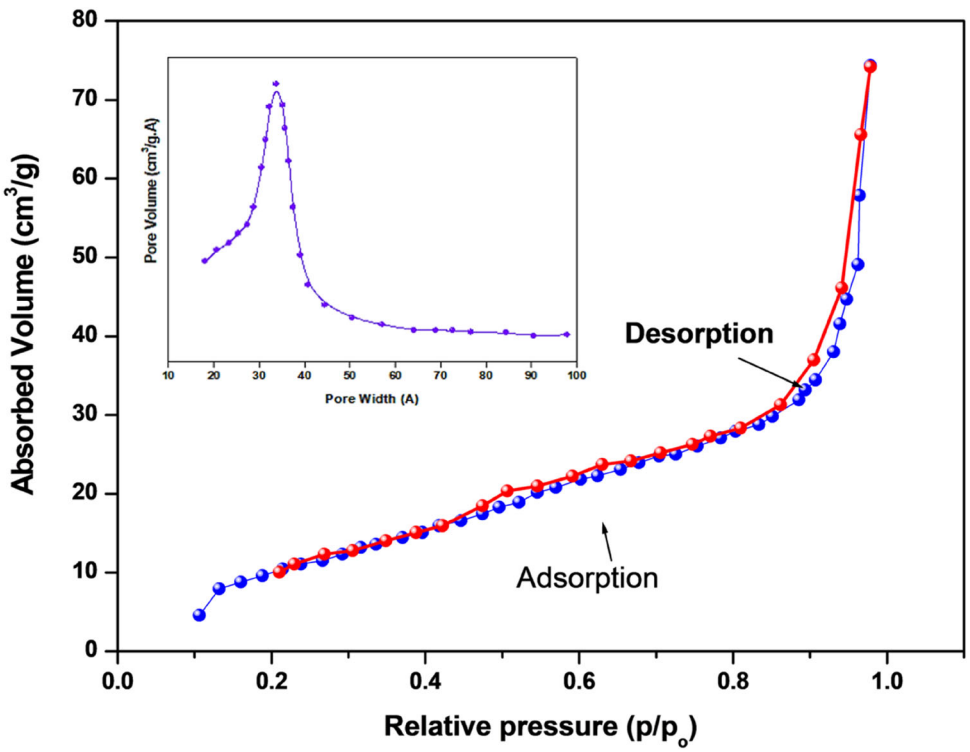

Fig. 5 N_2 adsorption/desorption isotherm of the synthesized ZnO NP and pore volume curves(inset)

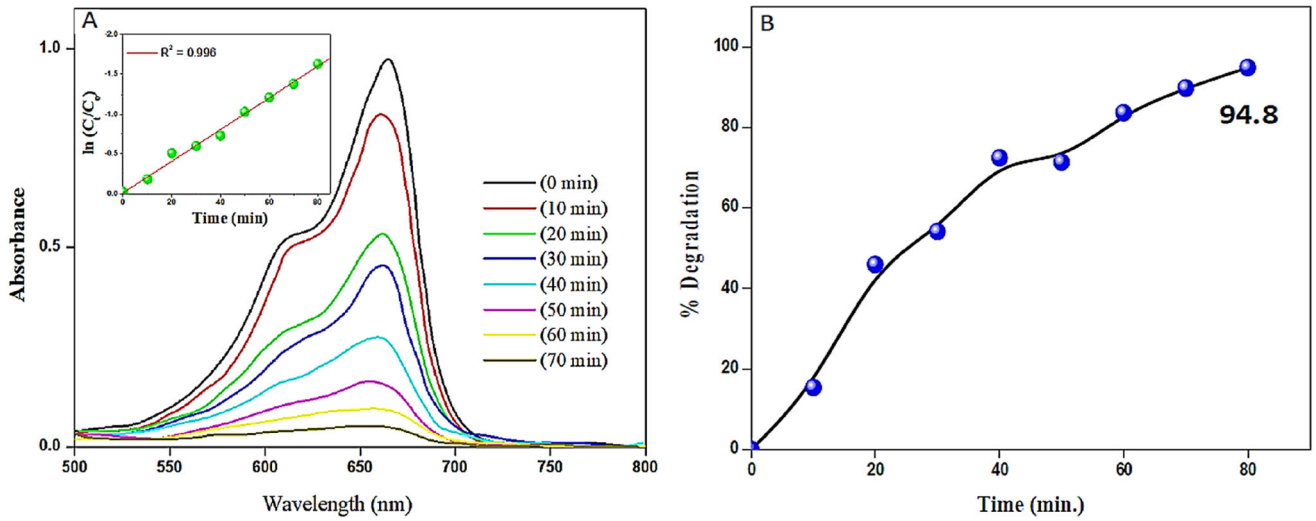

Fig. 6 **a** Photocatalytic activity of synthesized ZnO NPs and inset image shows a plot of -ln (C/C_0) versus t of ZnO nanoparticles **b** Time profile of MBdyedegradationefficiency(η)

the decolouration and open ring reaction. Then the reaction of photocatalytic activity of MB dye solution contains active species such as·OH (hydroxyl radicals), h^+ (holes), and $O_2^{\cdot -}$ (superoxideoxideradicalanion). Hydroxyl radicals, and Holes have an essential role in the degradation of MB dyes by Zinc oxide nanoparticles using UV light.

a. MB (aqueous solution) + ZnO → MB–ZnO
b. MB–ZnO + h v → MB–ZnO ($h^+ + e.^-$)
c. $e^- + O_2 \rightarrow O_2^{\cdot -}$
d. $h^+ + H_2O \rightarrow {}^{\cdot}OH + H^+$
e. MB–ZnO + h^+ /·OH /$O_2^{\cdot -}$→ ZnO + H_2O + CO_2 + by-products.

The adsorption kinetics of photodegradation exhibited pseudo-first-order kinetics. The rate Eq. (13) is given as

$$-\ln(C/C_0) = Kt \quad (13)$$

where C_0 is the first concentration of the MB dye solution,

C is the concentration after photodegradation,

K is the rate constant, and.

T is the time taken.

Degradation has occurred efficiently when the rate constant is less than 1. For reactant, the degradation rate is measured and found to be 0.3156 mg/L min. The high photocatalytic activity is due to the electrostatic interaction between the anionic methylene blue dye and the positive zeta potential of ZnO nanoparticles. Additionally, the physical interaction between the functional groups on the MB dye and the oxygen group of ZnO is the reason for the adsorption of MB dye effectively. Figure 6b presents the time profile of MB photocatalytic degradation efficiency. Around 45% of the total Methylene blue concentration was degraded within 20 min of the photocatalysis with a final Methylene blue degradation efficiency of 94% at the finish of 70 min, this implies a better dehydration process when compared to previously reported studies [49–52].

3.12 Hemolytic activity of ZnO NPs

Many bioactive molecules may concentrate on toxic problems known as hemolysis, which is characterized by the breakdown of human RBC (erythrocytes) which forms the hemoglobin. Damage to essential organs such as the heart, kidney, and liver was caused by the free hemoglobin in plasma. Then it is important to examine the hemolytic studies of the bio-active molecules. The hemolytic activity is considered the simple, inexpensive, and fast method for initial toxicity evaluation. Figure 7a shows the results of the hemolytic assay of positive control, negative control, and ZnO NPs. The percentage of lysis is 98.5% and 0.9% for positive and negative control respectively, while 125 μ g/mL of ZnO NPs exhibited 3.5% of total hemolytic activity and there was no destruction of red blood cells. The hemolytic activity of synthesized ZnO nanoparticles was less considerable, implying its safe nature in the chemotherapeutic

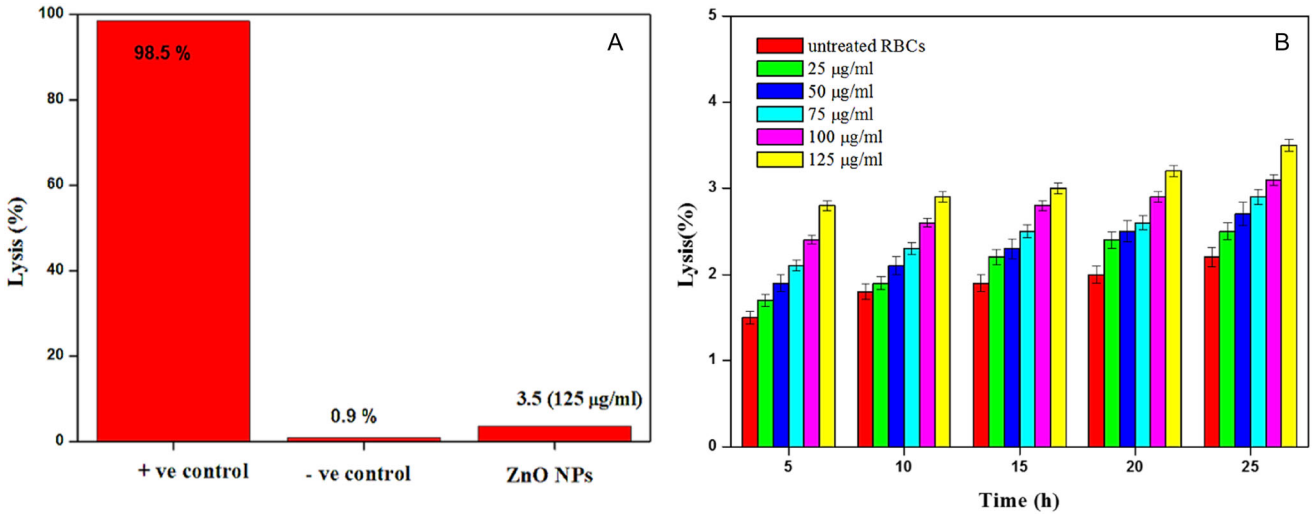

Fig. 7 **a** Haemolytic assay of synthesized ZnO NPs with controls-positive (Titron X-100) and negative control (PBS) **b** Haemolysis % of untreated RBCs and optimized sample at various ZnO NPs concentrations

application. Hemolytic activity was studied for various concentrations (25, 50, 75, 100, 125 μ g/mL) and compared with untreated RBCs (Fig. 7b). Both the number of dead cells and the concentration of ZnO NPs were increased and we observe the maximum hemolysis (3.5%) for 125 μ g/mL. Thus, a low concentration of nanoparticles can be used in pharmacological investigations due to their biocompatibility and non-toxic behavior.

3.13 Antioxidant activity of ZnO NPs

3.13.1 *Nitric oxide scavenging assay*

From this study, Fig. 8, results obtained show that the scavenging activity of NO (nitric oxide) increases with an equal increase of various concentrations (20–100 μ g/mL) for the Ascorbic acid, extract, and ZnO nanoparticles. The scavenging assay of the extract (85%) and ZnO NPs (70%) are lower when compared to ascorbic acid (90%) at 100 μ g/mL.

3.13.2 *H_2O_2 scavenging assay*

From this study, the results obtained show that the scavenging activity of H_2O_2 (hydrogen peroxide) increases with an equal increase of various concentrations (20–100 µg/mL) for the Ascorbic acid, extract, and ZnO NPs. The activity of the ascorbic acid (90%) and ZnO NPs (70%) are lower when compared to extract (85%) at 100 μ g/mL.

3.13.3 *DPPH free radical scavenging assay*

Antioxidant activity is dependent on the reducing influence of (2, 2-diphenyl-1-picrylhydrazyl) DPPH.

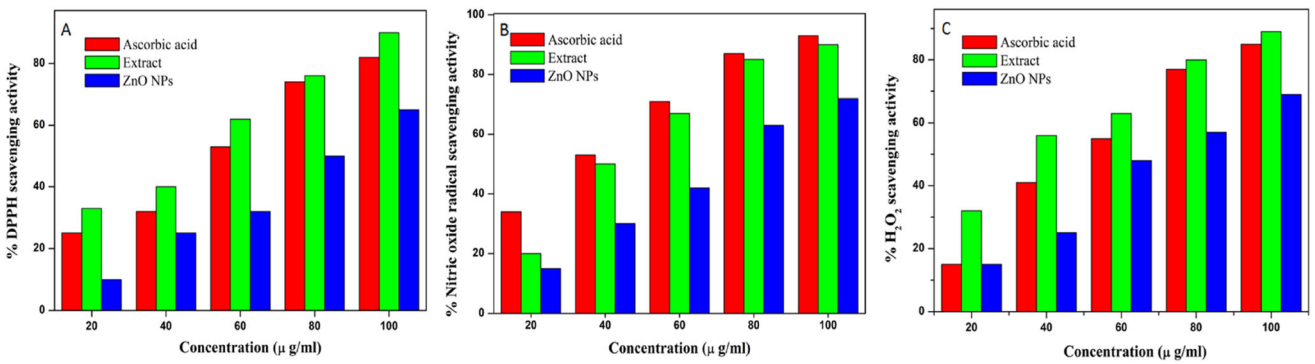

Fig. 8 RSA of prepared ZnO against **a** DPPH **b** Nitric oxide c H_2O_2 with various concentration

The green synthesized nanoparticles have excellent antioxidant activity, due to their small particle size with the larger surface area. ZnO NPs showed lower activity (65%) as compared to extract (90%) at 100 μ g/mL. The scavenging assay of ZnO NPs is low compared to the activity obtained with Ascorbic acid (Positive control). The activity increase with increasing concentration. Green synthesized ZnO NPs show good scavenging activity.

3.14 Electrochemical techniques

3.14.1 Cyclic voltammetry analysis

Figure 9a shows the CV curves for the rGO and rGO-ZnO nanocomposite using three types of electrodes in strong 2 M KOH electrolyte solution in the potential range (− 1 V to 1 V) at a scan rate (50 mV/s) shows quasi-rectangular shape. Figure 9b indicates the Cyclic Voltammetry curves of the entire composite at various scan rates. A quasi-rectangular shape of the CV curve without clear redox peaks indicates the perfect capacitance performance. According to equation (*a*), the specific capacitances of rGO-ZnO nanocomposite are found to be 667, 560, 432, 372, 295, and 251 F g^{-1} at 5, 10, 20, 50, and 100 mVs^{-1} respectively. Furthermore, the specific capacitance of rGO is 153, 118, 97, 82, 74, and 59 F g^{-1} respectively (Fig. 9c). The values of specific capacitance observed for synthesized rGO-ZnO nanocomposite electrodes are larger when compared with the same reports obtained earlier (Table 1). The prepared rGO-ZnO nanocomposite has a very high specific capacitance is assigned to the more charge storage and higher accessibility of electrolyte towards the nanomaterials. Besides, rGO exhibits EDLC behavior with higher surface area and conductivity whereas due to the synergistic effect the rGO-ZnO nanocomposite possesses better charge storage indicating the capacitance nature of rGO-ZnO nanocomposite. The K^+ ions in the KOH electrolyte interact with rGO-ZnO to form rGO-ZnOK. The specific capacitance of nanocomposite decreases with an increase in the scan rate. This may be due to the movement of ions within the electrolyte solution increasing slowly and then that lowers with the ease and extent of the charge-storing process of the active material.

3.14.2 Chronopotentiometry analysis

Knowing about the GCD (Galvanostatic Charge–Discharge) analysis and then the electrochemical performance, the materials were analyzed by Chronopotentiometry using strong 2 M KOH as electrolyte with a two-electrode cell (2E). Figure 10a shows the straight and symmetrically triangular GCD curves of rGO-ZnO and rGO with excellent reversibility for outstanding carrier transport and ideal EDLC behavior for good electrochemical performance indicating fast current–voltage response for the superior reversible redox process. Figure 10b shows the curves (GCD) of rGO-ZnO nanocomposite at various current densities from 1 to 25 A g^{-1}. It shows an IR peak at 1 A g^{-1} (0.935 V) to little change (0.902 V) showing that for electrolyte and rGO-ZnO nanocomposite electrodes the internal ion transfer arises easily. The specific capacitance is calculated based on equation (*b*) for discharge curves for rGO-ZnO (Fig. 10c) are about 667, 552, 428, 363, 282, and 232 F g^{-1} when the current density is 1.0, 5.0, 10, 15, 20, and 25 A g^{-1}, which is several-fold higher than that of rGO (147, 106, 87, 72, 64, and 49 F g^{-1}). The superior performance of this nanocomposite is due to

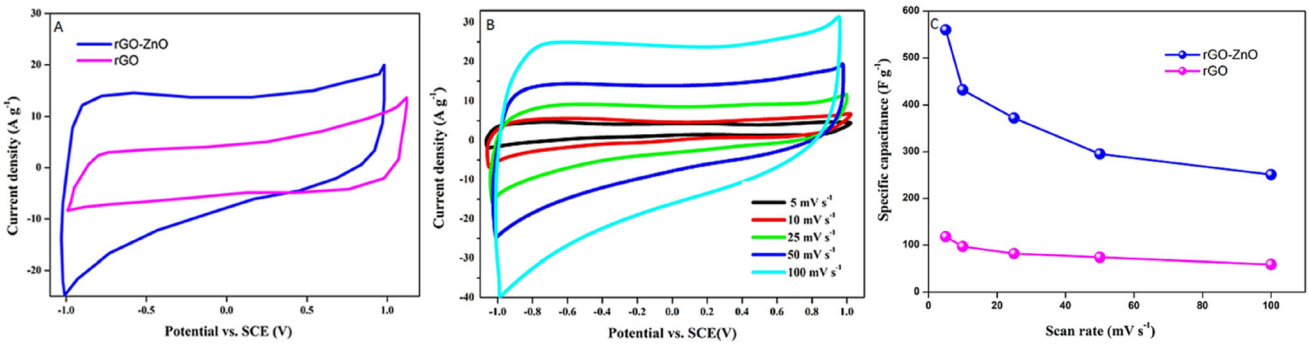

Fig. 9 **a** CV curves of rGO-ZnO nanocomposite and rGO at a scan rate of 50 mV s^{-1} **b** CV curves of ZnO-rGO based supercapacitor at different scan rates **c** Sc's of rGO-ZnO nanocomposite and rGO calculated at different scan rates

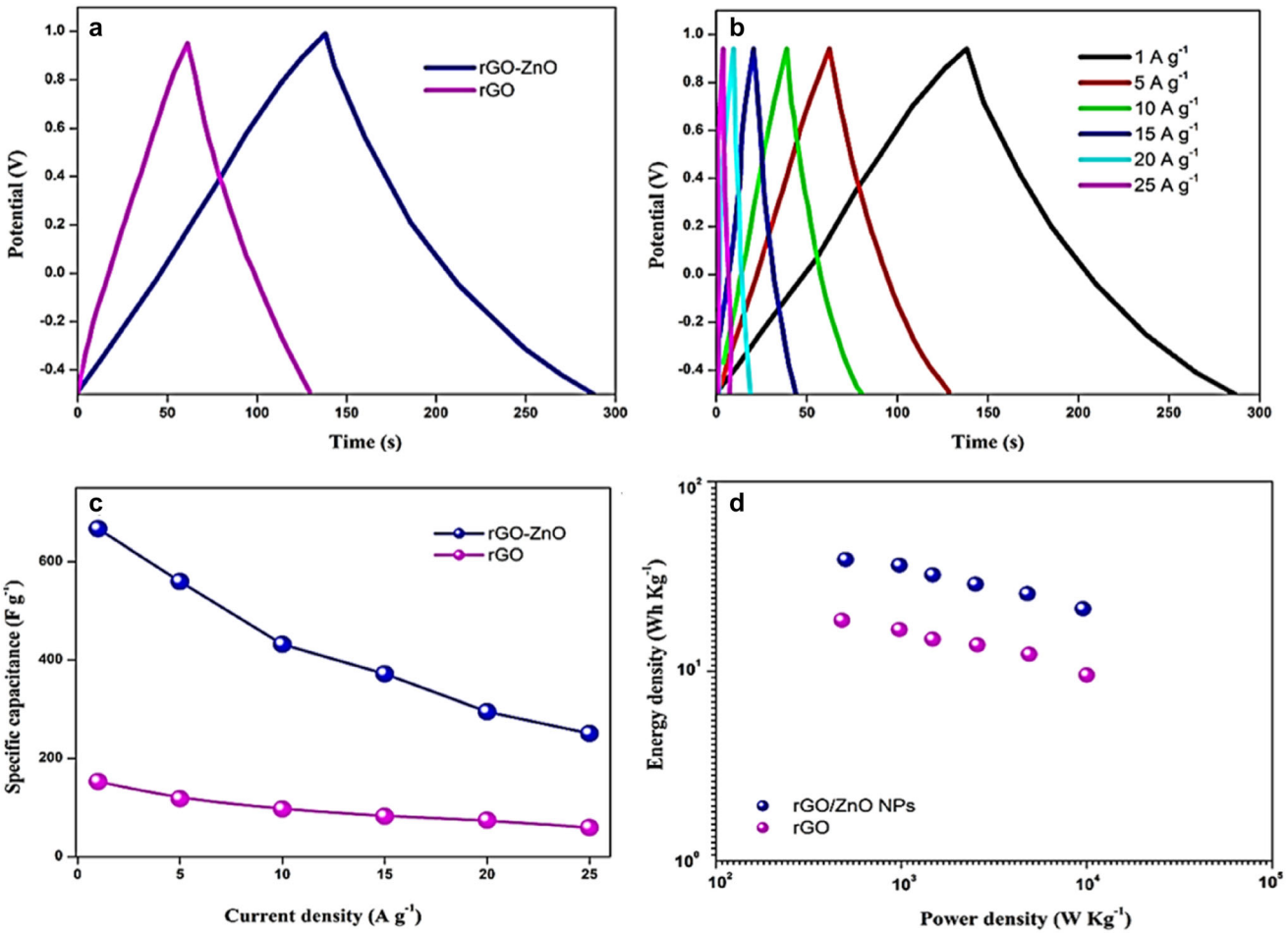

Fig. 10 **a** GCD curves of rGO-ZnO nanocomposite and rGO at 1 Ag^{-1}, **b** GCD curves of rGO-ZnO nanocomposite at different current densities, **c** Sc's of rGO-ZnO nanocomposite and rGO at different current densities, and **d** Ragone plots of rGO-ZnO nanocomposite and rGO

the morphology of the nanocomposite which helps the electrolyte ion transfer between electrode–electrolyte interface, the surface area of the nanocomposite which shortens the diffusion between the outer electrolytes to the inner surface and the defects are absent in rGO improves the electrical conductivity of rGO-ZnO nanocomposite which is suitable for higher electrical conductivity. The energy and power densities of rGO-ZnO nanocomposite material can be calculated from equations c and d using Ragone plots (Fig. 10d). The rGO-ZnO nanocomposite electrode shows the energy densities of 43.2, 37.2, 35.2, 32.6, 27.3, and 23.5 Wh kg^{-1} concerning the power densities of 500, 1000, 1500, 2500, 5000, and 10,000 W kg^{-1}. Similarly, rGO exhibit a maximum Energy density (d_e) of 20.3 Wh kg^{-1} is smaller than rGO-ZnO material.

3.14.3 *Electrochemical impedance spectroscopy*

The capacitive resistance behavior of the material based on frequency, the high charge transfer kinetics involved within the three types of the electrode and the electrolyte diffusion property, then AC impedance measurements were achieved. Nyquist plots (Fig. 11) of nanocomposite (rGO-ZnO) and the electrode (rGO) consist of a single straight line at the very low-frequency area due to the ideal electrical double-layer capacitive behaviour of the nanocomposite electrode and the semi-circle at the high-frequency area is obtained because of charge transfer resistance (Rct). Similarly, in a short 45° regime, the intermediate frequency is known as the Warburg impedance region due to the frequency-dependent ion transport or ion diffusion of the electrolyte in the electrode. To

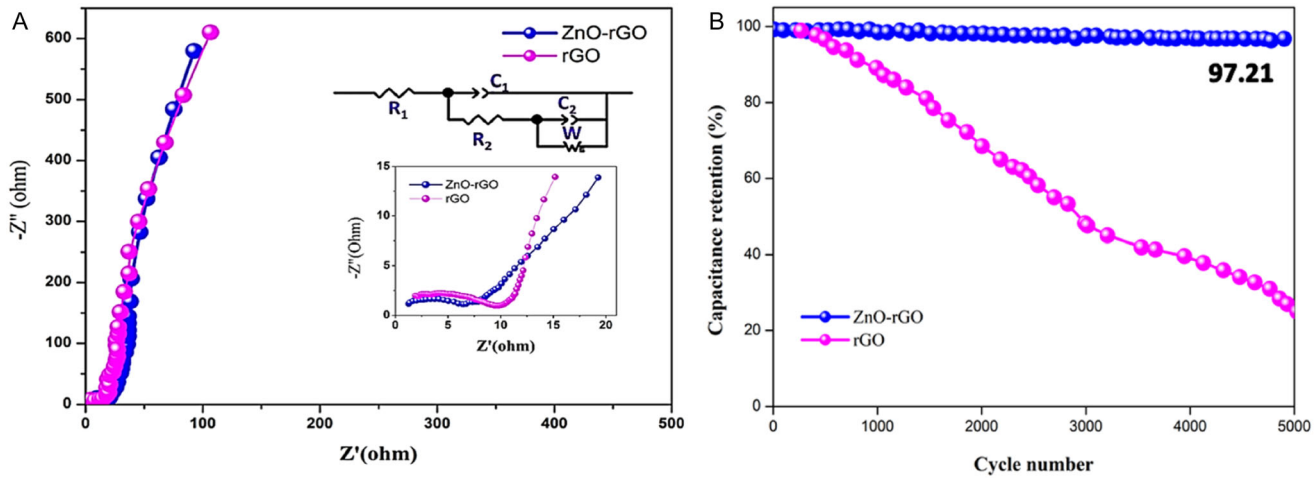

Fig. 11 **a** Nyquist plots of rGO and ZnO-rGO nanocomposite **b** Specific capacitances versus the cycle number of rGO and ZnO-rGO nanocomposites at a current density of 10 Ag^{-1}

illustrate the magnitude of equivalent series resistance, the diameter of the semi-circle is acquired from the high-frequency range (inset) from the x-intercept. It is observed that a decrease in internal resistance and increase in conductivity for smaller equivalent series resistance value of rGO-ZnO (4.3 Ω) than rGO (5.2 Ω). The inset of (Fig. 11) describes the equivalent circuit of the series of the electronic element including R_1 (electrolyte resistance) between the reference and working electrode and R_2 (Rct).

To evaluate the practical applications of electrochemical supercapacitor electrodes, then we tested the long-term cycling stability. To analyze the electrochemical stability of the nanocomposite electrode (rGO-ZnO) and rGO electrode, galvanostatic charge–discharge cycling tests tested the current density at 10 A g^{-1} for 5000 cycles. Figure 11 presents the specific conductance as a function of cycle number. rGO-ZnO nanocomposite electrode exhibit outstanding cycling stability with a capacitance retention of 97.2% after 5000 cycles suggesting that the prepared rGO-ZnO nanocomposite has a good potential for supercapacitor applications over another method ZnO material (Table 2). This is mainly due to the good mechanical stability, flexibility, and perfect hybridization of nanocomposite electrodes (ZnO and rGO).

4 Conclusion

The synthesis of ZnO NPs was successfully synthesized in a greener method (*L. nepetifolia* extract) and analyzed by UV–Vis absorption spectrum showing the blue shift when compared to bulk ZnO which is assigned to the size effect. FTIR of ZnO NPs appears the band at 500 nm is due to vibration of Zn–O bonding. The XRD pattern confirms that the synthesized ZnO NPs exhibit sphericality while zinc and oxide ions are present in the nanoparticles as

Table 2 Comparison of the specific capacitance of composite electrode material from earlier reports

Material	Electrolyte	Specific capacitance (F g^{-1})	Reference
rGO-ZnO	KOH	180	[53]
ZnO-rGO	$NaHCO_3$	63	[54]
ZnO- rGO	H_2O	432	[55]
rGO-ZnO	NaOH	41	[56]
ZnO- rGO	NaOH	188	[57]
rGO-ZnO	Na_2SO_4	448	[58]
rGO-ZnO	KOH	667	This work

observed by EDX analysis. The nanoparticles are fully agglomerated and the average size of ZnO NPs is about 26 nm were confirmed by SEM and TEM images respectively and matched with XRD crystallite size. ZnO NPs show good photocatalytic against methylene blue with 90% degradation. And it reveals excellent hemolytic activity for medicinal field applications and antioxidant assay against DPPH, Nitric oxide, and H_2O_2. The combined effect of ZnO and rGO shows the good electrochemical performance of the prepared (rGO/ZnO) nanocomposite electrode material when compared to pure ZnO. Nanocomposite electrode material reveals a high specific capacitance (667 F g^{-1}) and high cyclic stability. Therefore, the prepared ZnO nanomaterial can be widely used as an electrode material for applications in energy storage, in the nanomedicine field, and good dye degradation processes.

Acknowledgements

We thank Prof. N. Kumaraguru, and N. Samiveerappa, Bharathidasan University for supporting biological and electrochemical studies.

Author contributions

JM: Data collection, Data curation, Investigations, writing-original draft, Formal analysis, GP: investigations, writing-draft, Formal analysis, DA: investigations, Formal analysis S: supervision, validation, visualization, conceptualization, ASk: supervision, conceptualization, validation, visualization. The authors have fully read and approved the final version of the manuscript.

Funding

The authors have not disclosed any funding.

Data availability

The datasets generated during and /or analysed during the current study are available from the corresponding author on reasonable request.

Declarations

Competing interests The authors declared that they have no competing interests.

References

1. S. Vijayakumar, B. Vaseeharan, B. Malaikozhundan, M. Shobiya, Laurus nobilis leaf extract mediated green synthesis of ZnO nanoparticles: characterization and biomedical applications. Biomed. Pharmacother. **84**, 1213–1222 (2016)
2. J. Yan, J. Wang, L. Zhu, J. Wu, Green synthesis and characterization of zinc oxide nanoparticles using carboxylic curdlan and their interaction with bovine serum albumin. RSC Adv. **6**, 77752–77759 (2016)
3. A.N. Deva Krupa, R. Vimala, Evaluation of tetraethoxysilane (TEOS) sol-gel coatings, modified with green synthesized Zinc oxide nanoparticles for combating microfouling. Mater. Sci. Eng. C. **61**, 728–735 (2016)
4. F.T. Thema, E. Manikandan, M.S. Dhlamini, M. Maaza, Green synthesis of ZnO nanoparticles via Agathosma betulina natural extract. Mater Lett. **161**, 124–127 (2015)
5. F.M. Arvanaga, A. Bayramia, A. Habibi-Yangjehb, S.R. Pouran, A comprehensive study on antidiabetic and antibacterial activities of ZnO nanoparticles biosynthesized using Silybum marianum L seed extract. Mater. Sci. Eng C. **97**, 397–405 (2019)
6. K. Muhil Eswari, S. Asaithambi, M. Karuppaiah, P. Sakthivel, V. Balaji, D.K. Ponelakkia, R. Yuvakkumar, P. Kumar, N. Vijayaprabhu, G. Ravi, Green synthesis of ZnO nanoparticles using Abutilon Indicum and Tectona Grandis leaf extracts for evaluation of anti-diabetic, anti-inflammatory and in-vitro cytotoxicity activities. Ceram. Int. **48**(22), 33624–33634 (2022). https://doi.org/10.1016/j.ceramint.2022.07.308
7. Vaikundamoorthy Ramalingam, Pavithra Muthukumar Sathya, Thimmarayan Srivalli, Harshavardhan Mohan, Synthesis of quercetin functionalized wurtzite type zinc oxide nanoparticles and their potential to regulate intrinsic apoptosis signaling pathway in human metastatic ovarian cancer. Life Sci. **309**, 121022 (2022). https://doi.org/10.1016/j.lfs.2022.121022
8. M.S.S. Danish, A. Bhattacharya, D. Stepanova, A. Mikhaylov, M.L. Grilli, M. Khosravy, T. Senjyu, A systematic review of metal oxide applications for energy and environmental sustainability. Metals **10**(12), 1604 (2020). https://doi.org/10.3390/met10121604
9. B.E. Al-Jumaili, Fabrication and photoresponsive characteristics of ZnO film for ultraviolet ZnO/porous Si

photodetector: The effect of post-processing treatment. Opt. Mater. **133**, 112897 (2022). https://doi.org/10.1016/j.optmat.2022.112897

10. M. Busilă, V. Musat, R. Dinică, D. Tutunaru, A. Pantazi, D. Dorobantu, D.C. Culită, M. Enăchescu, Antibacterial and photocatalytic coatings based on Cu-Doped ZnO nanoparticles into microcellulose matrix. Materials **15**(21), 7656 (2022). https://doi.org/10.3390/ma15217656
11. Maha G. Batterjee, Arshid Nabi, Majid Rasool Kamli, Khalid Ahmed Alzahrani, Ekram Y. Danish, Maqsood Ahmad Malik, Green hydrothermal synthesis of zinc oxide nanoparticles for UV-light-induced photocatalytic degradation of ciprofloxacin antibiotic in an aqueous environment. Catalysts **12**(11), 1347 (2022). https://doi.org/10.3390/catal12111347
12. M.E. Awatif, Omran, Characterization of green route synthesized zinc oxide nanoparticles using Cyperus rotundus rhizome extract: Antioxidant, antibacterial, anticancer, and photocatalytic potential. J. Drug Deliv. Sci. Technol. **9**, 104000 (2022). https://doi.org/10.1016/j.jddst.2022.104000
13. F. Rahman, M.A. Majed Patwary, M.A. Bakar Siddique, M.S. Bashar, M.A. Haque, B. Akter, R. Rashid, M.A. Haque, A.K.M. Royhan Uddin, Green synthesis of zinc oxide nanoparticles using Cocos nucifera leaf extract: characterization, antimicrobial, antioxidant and photocatalytic activity. Royal Soc. Open Sci. (2022). https://doi.org/10.1098/rsos.220858
14. Tarek M. Abdelghany, Aisha M. H. Al-Rajhi, Reham Yahya, Marwah M. Bakri, Mohamed A. Al, Rana Yahya Abboud, Husam Qanash, Abdulrahman S. Bazaid, Salem S. Salem, Phytofabrication of zinc oxide nanoparticles with advanced characterization and its antioxidant, anticancer, and antimicrobial activity against pathogenic microorganisms. Biomass Conv. Bioref. **12**, 5 (2022). https://doi.org/10.1007/s13399-022-03412-1
15. S.O. Ogunyemi, Y. Abdallah, M. Zhang, H. Fouad, X. Hong, E. Ibrahim, M.I.A. Masum, A. Hossain, Jianchu Mo, Bin Li, Green synthesis of Zinc oxide nanoparticles using different plant extracts and their antibacterial activity against Xanthomonas oryzae pv. Oryzae. Artif Cells Nanomed. Biotechnol. **47**, 341–352 (2019)
16. H. Agarwal, S. Venkat Kumar, S. Rajeshkumar, A review on green synthesis of zinc oxide nanoparticles—an eco-friendly approach. Resour-Effi Technol. **3**, 406–413 (2017)
17. J.T. Adeleke, V. Theivasanthi, M. Thiruppathi, M. Swaminathan, T. Akomolafe, A.B. Alabi, Photocatalytic degradation of methylene blue by ZnO/ $NiFe_2O_4$ nanoparticles. Appl. Surf. Sci. **455**, 195–200 (2018)
18. F. Davar, A. Majedi, A. Mirzaei, Green synthesis of ZnO nanoparticles and its application in the degradation of some dyes. J. Am. Ceram. Soc. **98**, 1739–1746 (2015)
19. T.V. Surendra, S.M. Roopan, M.V. Arasu, N.A. Al-Dhabi, M. Sridharan, Phenolic compounds in drumstick peel for the evaluation of antibacterial, hemolytic and photocatalytic activities. J. Photochem. Photobiol. B: Bio. **161**, 463–471 (2016)
20. P. Thatoi, R. Kerry, S. Gouda, G. Das, K. Pramanik, H. Thatoi, J. Patra, Photo-mediated green synthesis of silver and zinc oxide nanoparticles using aqueous extracts of two mangrove plant species, *Heritiera fomes* and *Sonneratia apetala* and investigation of their biomedical applications. J. Photochem. Photobiol. B: Bio. **163**, 311–318 (2016)
21. R. Javed, M. Usman, S. Tabassum, M. Zia, Effect of capping agents: Structural, optical and biological properties of ZnO nanoparticles. Appl Surf Sci. **386**, 319–326 (2016)
22. M.V. Arasua, A. Madankumarb, J. Theerthagiric, S. Sallad, S. Prabu, Synthesis and characterization of ZnO nanoflakes anchored carbon nanoplates for antioxidant and anticancer activity in MCF7 cell lines. Mater. Sci. Eng C. **102**, 536–540 (2019)
23. G. Sharmila, M. Thirumarimurugan, C. Muthukumaran, Green synthesis of ZnO nanoparticles using Tecoma castanifolia leaf extract: Characterization and evaluation of its antioxidant, bactericidal and anticancer activities. Microchem. J. **145**, 578–587 (2019)
24. R.S. Ray, B. Sarma, M. Misra, Random shaped ZnO supported on a porous substrate as supercapacitor. Mater. Lett. **155**, 102–105 (2015)
25. D. Ponnamma, J.-J. Cabibihan, M. Rajan, S. Sundar Pethaiah, K. Deshmukh, J.P. Gogoi, S.K. Khadheer Pasha, M. Basheer Ahamed, J. Krishnegowda, B.N. Chandrashekar, A. Reddy Plu, C. Cheng, Synthesis, optimization and applications of ZnO/Polymer nanocomposites. Mater. Sci. Eng C. **98**, 1210–1240 (2019)
26. H. Raj Pant, B. Pant, H. Joo Kim, A. Amarjargal, C. Hee Park, L.D. Tijing, E. Kyo Kim, C. Sang Kim, A green and facile one-pot synthesis of Ag-ZnO/RGO nanocomposite with effective photocatalytic activity for removal of organic pollutants. Ceram. Inter. **39**, 5083–5091 (2013)
27. I.Y.Y. Bu, R. Huang, One-pot synthesis of ZnO/reduced graphene oxide nanocomposite for supercapacitor applications. Mater. Sci. Semiconduct. Process. **31**, 131–138 (2015)
28. Y. Haldoria, W. Voit, J.-J. Shim, Nano ZnO@reduced graphene oxide composite for high performances supercapacitor: green synthesis in supercritical fluid. Electrochim. Acta. **120**, 65–72 (2014)
29. J. Jayachandiran, J. Yesuraj, M. Arivanandhan, A. Raja, S.A. Suthanthiraraj, R. Jayavel, D. Nedumaran, Synthesis and electrochemical studies of rGO/ZnO nanocomposite for supercapacitor application. J. Inorg. Organomet. Polym. Mater. **28**, 2046–2055 (2018)

30. K. Elumalai, S. Velmurugan, Green synthesis, characterization and antimicrobial activities of zinc oxide nanoparticles from the leaf extract of Azadirachta indica (L.). Appl Surf Sci. **345**, 329–336 (2015)
31. R. Dobrucka, J. Długaszewska, Biosynthesis and antibacterial activity of ZnO nanoparticles using Trifolium pratense flower extract. Saudi J. Biol. Sci. **23**, 517–523 (2016)
32. K. Elumalai, S. Velmurugan, S. Ravi, V. Kathiravan, S. Ashokkumar, Green synthesis of zinc oxide nanoparticles using Moringa oleifera leaf extract and evaluation of its antimicrobial activity. Spectrochim. Acta.:Part A: Mol. Biomol. Spectrosc. **143**, 158–164 (2015)
33. A.A. Barzinjy, H.H. Azeez, Green synthesis and characterization of zinc oxide nanoparticles using *Eucalyptus globulus Labill*. leaf extract and zinc nitrate hexahydrate salt. SN Appl. Sci. **2**, 1–14 (2020)
34. R. Ramanarayanan, N.M. Bhabhina, M.V. Dharsana, C.V. Nivedita, S. Sindhu, Green synthesis of zinc oxide nanoparticles using extract of Averrhoa bilimbi(L) and their photoelectrode applications. Mater Today: Proceed. **5**, 16472–16477 (2018)
35. T. Karnan, S.A.S. Selvakumar, Biosynthesis of ZnO nanoparticles using rambutan (*Nephelium lappaceum* L.) peel extract and their photocatalytic activity on methyl orange dye. J. Molecul Struc. **1125**, 358–365 (2016)
36. H. Abdul Salam, R. Sivaraj, R. Venckatesh, Green synthesis and characterization of zinc oxide nanoparticles from *Ocimum basilicum* L. var. purpurascens Benth-Lamiaceae leaf extract. Mater Lett. **131**, 16–18 (2014)
37. S. Alamdari, M. Ghamsari, C. Lee, W. Han, H. Park, M.J. Tafreshi, H. Afarideh, M.H. Ara, Preparation and characterization of zinc oxide nanoparticles using leaf extract of *Sambucus ebulus*. Appl. Sci. **10**, 1–19 (2020)
38. H. Chandra, D. Patel, P. Kumari, J.S. Jangwan, S. Yadav, Phyto-mediated synthesis of zinc oxide nanoparticles of *Berberis aristata*: Characterization, antioxidant activity and antibacterial activity with special reference to urinary tract pathogens. Mater Sci. Eng C. **102**, 212–220 (2019)
39. M. Sundrarajan, S. Ambika, K. Bharathi, Plant-extract mediated synthesis of ZnO nanoparticles using *Pongamia pinnata* and their activity against pathogenic bacteria. Adv. Powder Technol. **26**, 1294–1299 (2015)
40. A. Diallo, B.D. Ngom, E. Park, M. Maaza, Green synthesis of ZnO nanoparticles by *Aspalathus linearis*: structural & optical properties. J. Alloy Compd. **646**, 425–430 (2015)
41. M. Silambarasan, S. Saravanan, T. Soga, Raman and photoluminescence studies of Ag and Fe-doped ZnO nanoparticles. Int. J. ChemTech Res. **7**, 1644–1650 (2015)
42. A. Erazo, S. Mosquera, J.E. Rodríguez-Paez, Synthesis of ZnO nanoparticles with different morphology: study of their antifungal effect on strains of *Aspergillus niger* and Botrytis cinerea. Mater. Chem. Phys. **234**, 172–184 (2019)
43. M.S. Geetha, H. Nagabhushana, H.N. Shivananjaiah, Green mediated synthesis and characterization of ZnO nanoparticles using Euphorbia Jatropa latex as reducing agent. J. Sci: Adv Mater. Dev. **1**, 301–310 (2016)
44. R. Pandimurugan, S. Thambidurai, Novel seaweed capped ZnO nanoparticles for effective dye photodegradation and antibacterial activity. Adv Powder Technol. **27**, 1062–1072 (2016)
45. D. Sharma, M. Sabela, S. Kanchi, P. Mdluli, G. Singh, T.A. Stenstrom, K. Bisetty, Biosy21nthesis of ZnO nanoparticles using Jacaranda mimosifolia flowers extract: synergistic antibacterial activity and molecular simulated facet specific adsorption studies. J. Photochem. Photobiol. B: Bio. **162**, 199–207 (2016)
46. N.S. Pavithra, K. Lingaraju, G.K. Raghu, G. Nagaraju, Citrus maxima (Pomelo) juice mediated eco-friendly synthesis of ZnO nanoparticles: applications to photocatalytic, electrochemical sensor and antibacterial activities. Spectrochim. Acta. Part A: Mol. Biomol. Spectrosc. **185**, 11–19 (2017)
47. P.P. Mahamuni, P.M. Patil, M.J. Dhanavade, M.V. Badiger, P.G. Shadija, A.C. Lokhande, R.A. Bohara, Synthesis and characterization of zinc oxide nanoparticles by using polyol chemistry for their antimicrobial and antibiofilm activity. Biochem. Biophy. Rep. **17**, 71–80 (2019)
48. D. Badma Priya, D. Thirumalai, I.V. Asharani, Influence of synthetic parameters on the enhanced photocatalytic properties of ZnO nanoparticles for the degradation of organic dyes: a green approach. Mater. Sci.: Mater. Electron. **32**, 9956–9971 (2021)
49. S. Vasantharaj, S. Sathiyavimal, P. Senthilkumar, V.N. Kalpana, G. Rajalakshmi, M. Alsehli, A. Elfasakhany, A. Pugazhendhi, Enhanced photocatalytic degradation of water pollutants using bio-green synthesis of zinc oxide nanoparticles (ZnO NPs). J. Environ. Chem. Eng. **9**, 105772 (2021). https://doi.org/10.1016/j.jece.2021.105772
50. H. Sadiq, F. Sher, S. Sehar, E.C. Lima, S. Zhang, H.M.N. Iqbal, F. Zafar, M. Nuhanovic, Green synthesis of ZnO nanoparticles from Syzygium Cumini leaves extract with robust photocatalysis applications. J. Mol. Liq. **335**, 116567 (2021). https://doi.org/10.1016/j.molliq.2021.116567
51. T.S. Aldeen, H.E.A. Mohamed, M. Maaza, ZnO nanoparticles prepared via a green synthesis approach: physical properties, photocatalytic and antibacterial activity. J. Phys. Chem. Solids **160**, 110313 (2022). https://doi.org/10.1016/j.jpcs.2021.110313
52. S. Venkatesan, S. Suresh, P. Ramu, J. Arumugam, S. Thambidurai, N. Pugazhenthiran, Methylene blue dye degradation

potential of zinc oxide nanoparticles bioreduced using Solanum trilobatum leaf extract. Res. Chem. **4**, 100637 (2022)
53. C. Kalaiarasi, P.S. Pragathiswaran, Green chemistry approach for the functionalization of reduced graphene and ZnO as efficient supercapacitor application. J. Mol. Struct. (2021). https://doi.org/10.1016/j.molstruc.2021.130704
54. S. Yadav, N. Rani, K. Saini, Green synthesis of ZnO and CuO NPs using *Ficus benghalensis* leaf extract and their comparative study for electrode materials for high performance supercapacitor application. Materi. Today: Proc. **49**, 2124–2130 (2022)
55. J. Li et al., Green synthesis of cellulose/graphene oxide/ZIF8 derived highly conductivity integrated film electrode for supercapacitor. Carbon **185**, 599–607 (2021)
56. K.S. Lee, I. Phiri, J.H. Park, J.M. Ko, S.H. Kim, Novel structure of bacteria doped ZnO particles: facile and green synthesis route to prepare hybrid material for supercapacitor. J. Ind. Eng. Chem. **97**, 250–255 (2021)
57. Yunfu Liu, Guohui Liu, Green synthesis and electrochemical performances of ZnO/graphene Nanocomposites. Ionics **28**, 3547–3555 (2022)
58. M. Saini, Biosynthesized zinc oxide nanoparticles using seed and bark extract of Azadirachta indica for antibacterial, photocatalytic and supercapacitor applications. Mater. Sci. Eng., B **282**, 115789 (2022)